Acta Materialia 306 (2026) 121868

Contents lists available at ScienceDirect

Acta Materialia

journal homepage: www.elsevier.com/locate/actamat

Full length article

In situ TEM measurement of strain rate-dependent activation volume of ultrafine-grained Au films

Yichen Yang [a], Kunqing Ding [a], Xing Liu [c], Ting Zhu [a], Josh Kacher [b], Olivier Pierron [a,*]

[a] Woodruff School of Mechanical Engineering, Georgia Institute of Technology, Atlanta, GA 30332, USA
[b] School of Materials Science and Engineering, Georgia Institute of Technology, Atlanta, GA 30332, USA
[c] Department of Mechanical and Industrial Engineering, New Jersey Institute of Technology, Newark, NJ 07102, USA

ARTICLE INFO

Keywords:
MEMS
In situ TEM
Strain rate effect
Physical activation volume
Nanomechanical testing

ABSTRACT

Understanding the rate-controlling plastic deformation mechanisms in ultrafine-grained metals is essential for improving their mechanical performance. Strain rate sensitivity and the associated activation volume are commonly used to probe these underlying mechanisms. In this study, we investigate the strain rate-dependent deformation behavior of ultrafine grained gold films using an in situ transmission electron microscopy (TEM) nanomechanical testing technique. This approach enables direct measurement of the strain rate sensitivity and physical activation volume across a wide range of strain rates ($\sim 10^{-5}$ to 1 s^{-1}), while observing dynamic dislocation processes. The results reveal a marked decrease in strain rate sensitivity with increasing strain rate, accompanied by an increase in physical activation volume, suggesting a transition in the rate-limiting mechanisms. In situ TEM observations capture a transition from single-slip to multi-slip activity and the formation of dislocation junctions at higher strain rates. Integrated experimental and modeling analyses reveal that the rate-controlling mechanisms are governed not only by the external loading condition but also by the internal stress state, evidenced by transient dislocation dynamics and evolving dislocation structures observed through in situ TEM straining experiments.

1. Introduction

Nanocrystalline (NC) and ultrafine-grained (UFG) metals are known for their exceptional mechanical strength, but improving their overall mechanical performance requires a fundamental understanding of the underlying plastic deformation mechanisms [1]. Their high grain boundary (GB) density leads to a complex interplay between intragranular and GB-mediated deformation mechanisms [2,3]. However, the enhanced strength is often accompanied by reduced ductility, underscoring the need for a comprehensive understanding of these mechanisms to achieve a better strength-ductility balance. Several deformation mechanisms, including GB sliding, GB migration, twinning, and the emission of partial and full dislocations from GBs, have been reported in UFG and NC metals [4–14]. Despite extensive characterization of these mechanisms, determining the rate-controlling process remains a challenge [15,16]. Gaining deeper insight into how intergranular and GB-based mechanisms interplay is essential for designing NC and UFG metals with improved mechanical properties [17,18].

We recently conducted in situ TEM experiments to observe plastic deformation processes and measure the sample-level physical activation volume, V^* in NC and UFG metallic thin films [19–21]. This signature parameter of the rate-controlling deformation mechanisms reflects the number of atoms involved in overcoming the energy barrier during a stress-driven, thermally activated process [22]. We also used a model developed by Conrad [23] to correlate our experimental activation volumes to atomistically calculated values of candidate unit dislocation processes [24]. This model introduces a Hall-Petch-like relation to account for grain size effects and link the measured activation volume for a polycrystal to both intragranular and intergranular contributions. Our preliminary results on UFG Au thin films (average grain size ~ 140 nm) highlighted a discrepancy between experimental values of V^* (ranging from 5 to $10b^3$ [21]) and atomistic simulations of displacive dislocation nucleation mechanisms predicting larger activation volumes of 20 to $40b^3$ [24]. This discrepancy is further amplified when taking into accounts the grain size difference between experiments and models (140 vs 10 nm) via Conrad's Hall-Petch-like relation [24]. One possible explanation is the effect of applied strain rate on the experimental measurements and the increased influence of diffusive mechanisms [25,

* Corresponding author.
E-mail address: olivier.pierron@me.gatech.edu (O. Pierron).

https://doi.org/10.1016/j.actamat.2025.121868
Received 11 August 2025; Received in revised form 9 December 2025; Accepted 22 December 2025
Available online 23 December 2025

26].

This study addresses a critical gap in understanding the rate-controlling deformation mechanisms in UFG Au thin films by directly measuring sample-level physical activation volumes and observing active deformation processes as a function of applied strain rate. Leveraging recent advances in our MEMS-integrated TEM technique, previously applied to investigate plastic kinetics in Au thin films at low (i.e. 10^{-5}–10^{-4} s^{-1}) strain rates [21,27–29], we combine V^* measurements with in situ TEM observations across a wider range of strain rates, from 10^{-5} to 1 s^{-1}. Our integrated experimental and modeling analyses reveal the effects of strain rate and stress history on rate-controlling mechanisms, as reflected by transient dislocation activity and evolving dislocation structures observed through in situ TEM straining experiments. These results provide new insight into the interplay between external loading and internal stress states in governing rate-limiting mechanisms in UFG metals.

2. Experimental

2.1. Nanomechanical testing setup

Free-standing, dog-bone-shaped Au thin film microspecimens were fabricated using optical lithography, e-beam evaporation, lift-off, and XeF_2 etching of the Si substrate (see prior work for additional details on the specimen fabrication [27,29]). The specimens have a thickness of 100 nm and an average grain size of 142 nm, as measured from precession electron diffraction (PED) analysis in our previous study [30].

As shown in Fig. 1 (a-b), a thermal actuator, oxide bridge, specimen pad with a stationary beam, and load sensor are the main components of our MEMS device that is used to conduct mechanical tests [28]. The specimen is mounted on the specimen gap of our MEMS device by two small droplets of ultraviolet (UV) curable glue (Fig. 1(c)). Once the adhesive is cured under UV light, the specimen is firmly anchored and ready for mechanical tests. Resistive heating causes the thermal actuator to shift the center shuttle by a distance X_A when a voltage is applied across it. The distance between the thermal actuator and specimen, and the presence of an oxide bridge in between (with a thick layer of Si underneath the bridge) acting as a heat sink, leads to negligible temperature increase of the specimen [31]. The specimen is elongated, and the load sensor beams, with known stiffness (K_{LS}), are displaced by X_{LS}. Our recent improvements in the MEMS design [28] feature simultaneous stress and strain measurements solely from TEM imaging (as opposed to capacitive sensing from previous studies), thanks to a stationary beam located at the middle of the specimen gap allowing live measurements of both X_A and X_{LS}. Nominal engineering strain values are calculated knowing the specimen's gauge length, L, (freestanding part ~10 μm) and the measured X_A-X_{LS}. (X_A-X_{LS} / L). Local engineering strain values can also be calculated along the specimen's gauge length through edge feature tracking by digital image correlation [28]. Local engineering strains are lower and more accurate than the nominal values, due to finite elastic deformation in the clamp regions of the specimen [28,32].

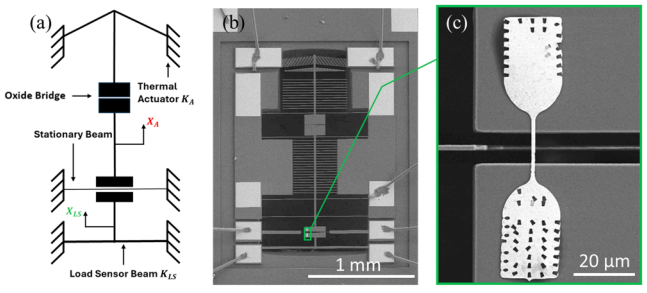

Fig. 1. (a) Schematic of the MEMS design. (b) SEM images of (b) the MEMS device, and (c) an untested specimen glued on the testing area.

These improvements enable testing at larger strain rates (up to 10^{-1} s^{-1}). The strain rate is not controlled during a test; instead, the rate of MEMS displacement (X_A) is. The resulting strain rate is calculated using the local strain values, at the onset of plastic deformation (plastic strain value of 0.2 %). Fig. 2 shows an example of a monotonic test of an Au thin film at a strain rate of 1.3 $\times$ 10^{-2} s^{-1}. Fig. 2(a) shows four selected TEM images of the entire specimen taken during tensile testing, from which X_A and X_{LS} can be measured with sub-nm resolution [28].

In this study, we investigate the effect of strain rate (measured at the onset of plastic deformation during the pre-loading) on the physical activation volumes (see Section 2.2), whose measurements are described next.

2.2. Activation volume measurements

Multiple transient experiments are performed to measure the physical activation volume of a thin film specimen using our MEMS technique. Each transient segment consists of applying a constant input voltage across the thermal actuator, and reloading to the same stress level (i.e., same initial X_{LS}) is done between two consecutive transient segments by increasing X_A accordingly. The physical activation volume is calculated using the following equation

$$V^* = kT\ln\left(\frac{\dot{\gamma}_{i2}/\dot{\gamma}_{f1}}{\Delta\tau_{12}}\right) = \sqrt{3}kT\ln\left(\frac{\dot{\varepsilon}_{pl,i2}/\dot{\varepsilon}_{pl,f1}}{\Delta\sigma_{12}}\right) \quad (1)$$

where $\dot{\gamma}_{f1}$ and $\dot{\gamma}_{i2}$ are the final and initial plastic shear strain rate of the first and second transient segments, respectively, $\Delta\tau_{12}$ is the shear stress increase during the reload, $\dot{\varepsilon}_{pl,i2}$, $\dot{\varepsilon}_{pl,f1}$, and $\Delta\sigma_{12}$ correspond to the initial and final normal plastic strain rates, and the normal stress increase, respectively, k is the Boltzmann constant and T is the absolute temperature.

With our new image-based sensing, we observed that, during a transient segment (input voltage across the thermal actuator is constant), X_A is not strictly constant; instead a slight increase is measured. This is likely due to the response time needed for the whole MEMS device to reach thermal equilibrium. The effect of the evolving X_A on the plastic strain accumulation during the transient segments is now included, thereby improving the accuracy of our V^* measurements. The plastic strain accumulation during a transient segment, $\Delta\varepsilon_{pl}$, is given by Eq. (2), with the full derivation and a comparison with the previous approach provided in the Supplementary Information:

$$\Delta\varepsilon_{pl} = \frac{\Delta X_A - \Delta X_{LS}\left(\frac{K_{LS}}{K_S} + 1\right)}{L} \quad (2)$$

with ΔX_A and ΔX_{LS}, the evolution of X_A and X_{LS} during the transient segments, and K_S the specimen's stiffness (calculated from the initial portion of the test). For each transient segment, plastic strain rates were calculated by first fitting the plastic strain versus time using a logarithmic function (see Figure S1(a)) and taking the appropriate derivative values (i.e. at the end of the first transient segment, and at the beginning of the second one). Only the fits with R^2 over 0.95 were used. Calculating plastic strain evolution with Eq. (2) without assuming ΔX_A= 0 during a transient segment improves the accuracy of the V^* values (see Figure S1 for representative examples).

These activation volume measurements represent the miniaturized (MEMS-based) equivalent of larger scale mechanical measurements [33] and additionally allow concurrent in situ TEM observations. Traditional macro-scale testing machines enable two types of multiple transient experiments: stress relaxation (i.e., the specimen strain is held constant during the transients) or creep (i.e., the applied stress is constant during the transients). The current MEMS technique enables multiple transient experiments that are neither purely stress relaxation nor creep (see the Supplementary Information for additional details). Importantly, the

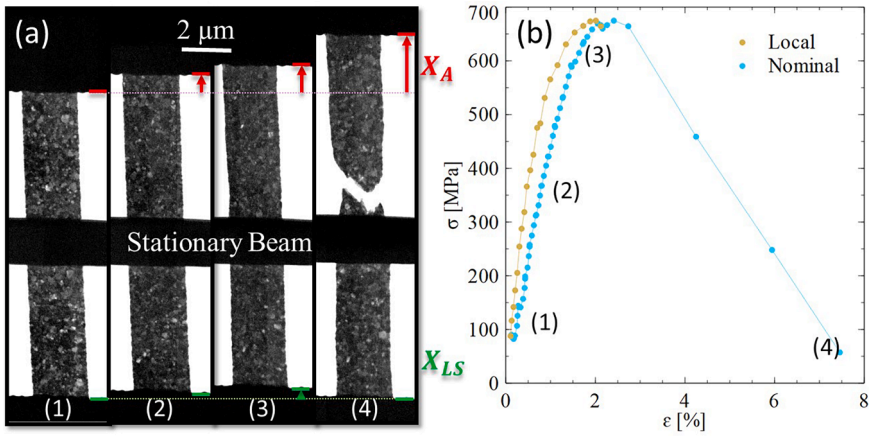

Fig. 2. (a) In situ bright-field TEM images taken during monotonic tensile testing at a strain rate of 1.3 $\times 10^{-2}$ s^{-1}, highlighting the measured quantities X_A and X_{LS}. (b) Stress-strain response based on either nominal or local strain, with corresponding images (1–4) shown in (a).

type of transient does not affect the measured physical activation volume [33], since in all these multiple transient experiments (regardless of the transient type), the stress dependence of dislocation velocity is probed.

3. Results

3.1. Strain rate sensitivity of UFG Au films

Twelve monotonic uniaxial tension tests were performed on 100 nm-thick UFG Au films to measure their mechanical properties across a wide range of strain rates, from 1.7 $\times 10^{-5}$ to 3 $\times 10^{-1}$ s^{-1}. The stress-strain curves (using local engineering strain values) from these tests are shown in Fig. 3(a). Over this range of strain rates, the yield stress increases approximately threefold, from 230 MPa to 721 MPa and the ultimate stress increases accordingly, indicating pronounced strain-rate dependent strengthening. However, this strengthening came at the cost of reduced ductility, reflecting a strain-rate-dependent trade-off between strength and plasticity. Post-fracture images in Fig. 4 further illustrates this trend. At a low strain rate of 1.7 $\times 10^{-5}$ s^{-1}, the film exhibited ~12.5 % ductility, with significant necking and gauge width reduction, indicative of substantial plastic deformation. In contrast, at a higher strain rate of 1.6 $\times 10^{-2}$ s^{-1}, the fracture surface appeared sharp and localized, with no visible necking, and the sample failed after only ~1.5 % elongation.

The strain rate sensitivity exponent m is typically determined by fitting a power law ($\sigma \propto \dot{\varepsilon}^m$) to the yield stress versus strain rate data [3–7]. Fig. 3(b) shows our yield stress and ultimate stress data versus strain rate, on logarithmic scales. A decrease in m with increasing $\dot{\varepsilon}$ is observed, which is similar to what was observed in another study on nanocrystalline Au films [25]. To better fit the data, we employed a logarithmic fit to capture the continuous variation in strain rate sensitivity, shown as the dotted lines in Fig. 3(b). Across the tested strain rate range, m gradually decreased from 0.16 to 0.04, indicating a smooth, progressive shift in deformation mechanisms rather than an abrupt change.

3.2. Physical activation volume measurement

3.2.1. Example of activation volume measurement

Fig. 5 shows an example of activation volume measurements using multiple transient segments for an Au thin film that was tested at a strain rate of 8 $\times 10^{-2}$ s^{-1}. The strain rate is the value measured at the onset of plastic deformation, prior to the multiple transient segments. Fig. 5(a) shows the overall stress-strain curve, with several transient segments performed at a stress level of around 550–600 MPa. Figs. 5(c)-(f) shows the plastic strain evolution during four different transient segments along with the logarithmic fits (black lines) used to determine plastic strain rate, from which three V^* values are obtained using Eq. (1) and plotted in Fig. 5(b) as a function of applied stress (value taken at the end of each reloading segment).

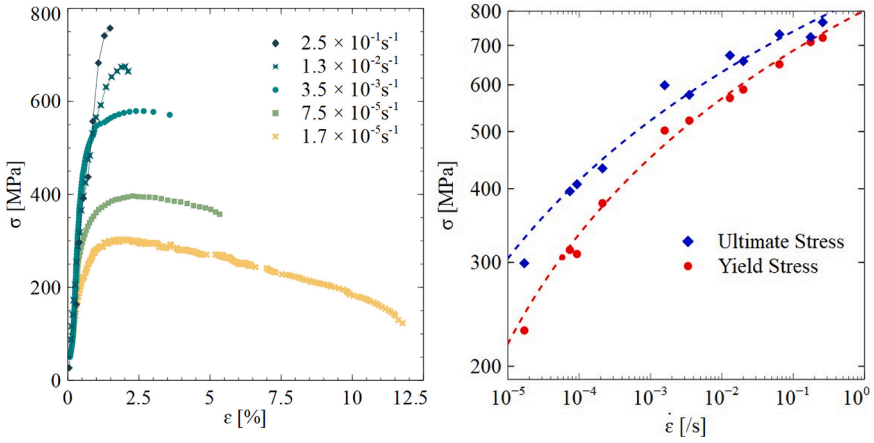

Fig. 3. (a) Stress as a function of strain for the specimens tested under different strain rates. (b) Corresponding yield stress and ultimate stress as a function of strain rate $\dot{\varepsilon}$, with log fits (dashed lines).

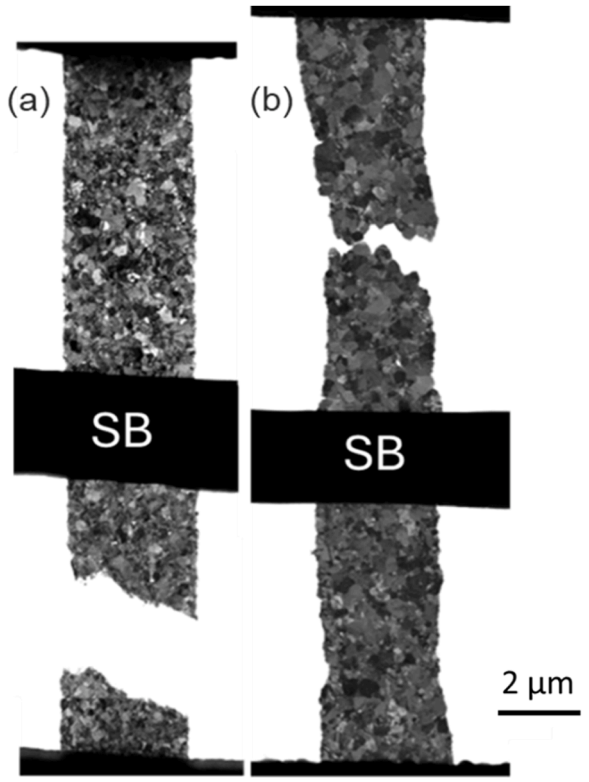

Fig. 4. Bright-field TEM images of fractured Au specimens after in situ TEM loading experiments at strain rates $\dot{\varepsilon}$ of (a) 1.6 $\times 10^{-2}$ s^{-1} and (b) 1.7 $\times$ 10^{-5} s^{-1}. The stress-strain curves associated with these tests are shown in Figure 3(a). SB: stationary beam.

3.2.2. Strain rate effect on physical activation volume

Activation volume measurements were performed on six different specimens for different strain rates (whose values are measured at the onset of plastic deformation, prior to the multiple transient segments) and stress levels ranging from 330 to 610 MPa. To facilitate the comparison, strain rates were classified as "low" (from 1 $\times 10^{-5}$ to 1 $\times$ 10^{-4} s^{-1}, three different specimens) or "high" (from 1 $\times$ 10^{-1} to 1 s^{-1}, three different specimens). It is notable that the initial strain rate strongly influences the subsequent relaxation behavior. High-rate loading consistently resulted in relaxation plastic strain rates on the order of 10^{-3} s^{-1}, while low-rate loading produced relaxation strain rates closer to 10^{-4} s^{-1}. This distinction reflects that the accessible relaxation mechanisms are modulated by the initial loading rate. Fig. 6 shows that the activation volumes obtained at low $\dot{\varepsilon}$ were consistently smaller than those obtained at high $\dot{\varepsilon}$, even when comparing activation volumes calculated at the same stress levels. Both high and low strain rate regimes exhibit stress-dependent V^*, with the V^* calculated at low $\dot{\varepsilon}$ displaying a less pronounced sensitivity to stress variations. Within the overlapping stress between two rates (380 to 480 MPa), V^* was calculated to be 8 to 12b^3 for low $\dot{\varepsilon}$ and 12 to 20 b^3 for high $\dot{\varepsilon}$. When considering the full stress range, the calculated V^* values ranged from 8 to 14b^3 for low $\dot{\varepsilon}$, and V^* extended from 6 to 20b^3 for high $\dot{\varepsilon}$ across their respective stress ranges of 330 to 490 MPa and 370 to 605 MPa.

3.3. Mechanistic observations

3.3.1. In situ TEM observations under low strain rates

To directly investigate the active deformation mechanisms, we conducted in situ TEM transient experiments under different strain rates and at similar stress levels used for V^* measurements. Each transient test lasted up to 10 min, allowing sufficient time to observe the active deformation processes.

Fig. 7 and the associated Video S1 show dislocation activity after the

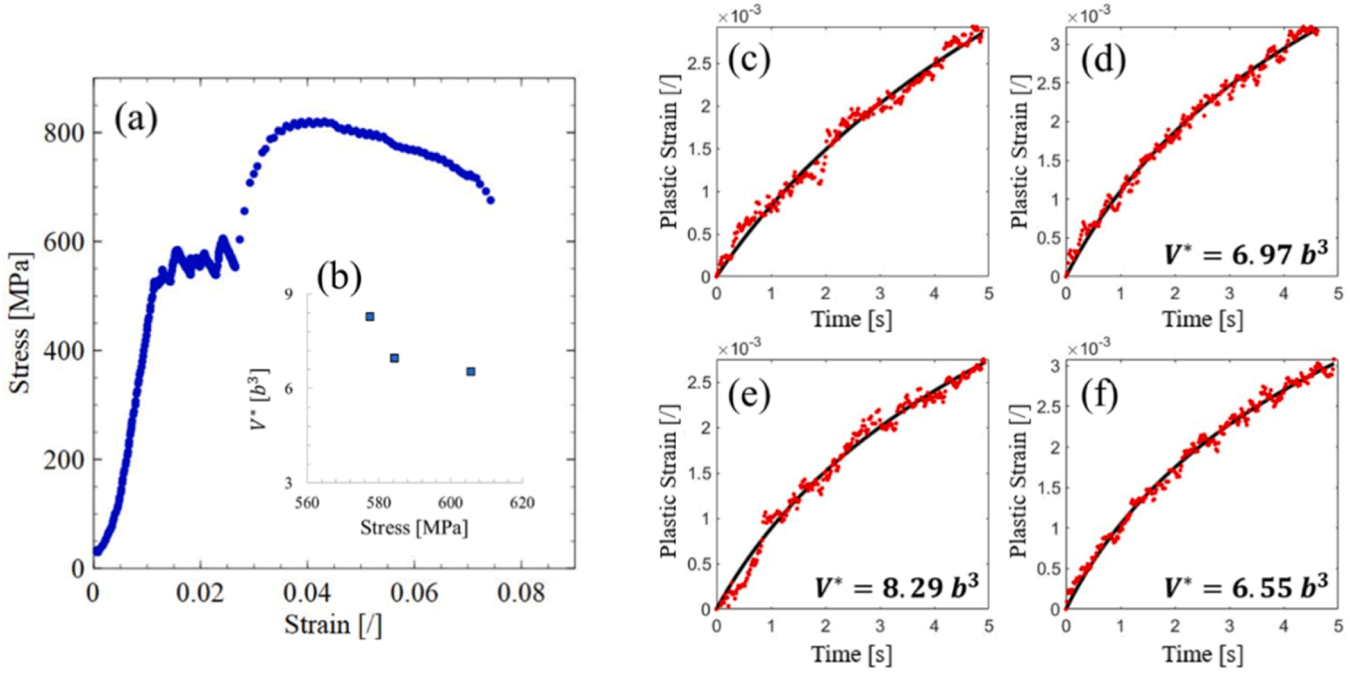

Fig. 5. Example of a multiple transient test conducted on a 100-nm-thick Au film at a strain rate of 8 $\times 10^{-2}$ s^{-1} (value measured at the onset of plastic deformation, prior to the multiple transient segments) (a) Stress-strain response during the test. (b) Calculated activation volume V^* values as a function of stress from 4 consecutive transient segments (each physical activation volume requires two consecutive segments). (c-e) Plastic strain evolution during the four transient segments (red symbols), overlaid with their logarithmic fits (black lines) used to determine plastic strain rate and the corresponding V^* values. The V^* shown in (d) is based on the transient segments shown in (c) and (d). The V^* shown in (e) is based on the transient segments shown in (d) and (e). The V^* shown in (f) is based on the transient segments shown in (e) and (f).

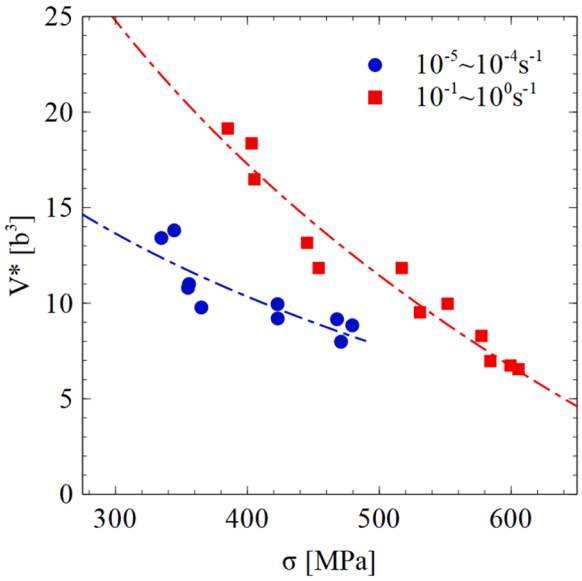

Fig. 6. Physical activation volume V^* as a function of stress σ for high and low strain rates (whose values are measured at the onset of plastic deformation, prior to the multiple transient segments) and their log fits (dashed lines).

applied stress reaches 350 MPa under a low strain rate of 1×10^{-4} s^{-1}, corresponding to a plastic strain of approximately 0.2 %. Multiple dislocations (indicated by arrows) emitted from a GB and propagated across the grain interior along a single slip system. Pre-existing dislocations within the grain remained immobile throughout the in situ TEM straining, and no additional slip systems were activated. Several dislocations were pinned at one of the GB, suggesting that the driving stress was insufficient to overcome the barrier for complete motion. This

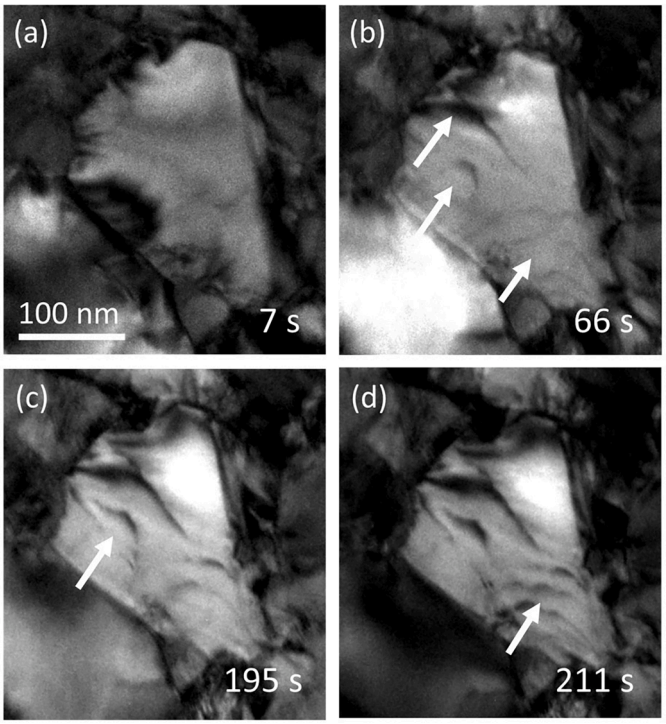

Fig. 7. In situ TEM images (a-d) showing activation of a single slip system during the transient period after loading to 350 MPa under a low strain rate of 1×10^{-4} s^{-1}. Arrows indicate moving dislocations. Additional dislocations were visible within the grain interior but remained immobile throughout the experiment. (Available in Video S1).

behavior, where dislocation motion was confined to a single slip system per grain, was consistently observed at low strain rates, independent of grain size.

3.3.2. *In situ TEM observations under high strain rates*

Fig. 8 shows the immediate and longer-term microstructural evolution after loading to ~600 MPa under a high strain rate of 1 s^{-1}, corresponding to a plastic strain of approximately 0.2 %. For these strain rates, the corresponding short duration of the experiment prevented switching from low magnification (for accurate stress and strain measurements) to high magnification (for TEM observations). Instead, the stress levels were estimated by first conducting an experiment at low magnification on a reference specimen with identical dimensions, and then repeating the same experimental conditions at high magnification on the test specimen. In Fig. 8, a rapidly evolving dislocation network was observed, with dislocations nucleating from multiple GBs within a single grain. The rapid dynamic response was in stark contrast to the typical subdued activity observed under low strain rate and stress conditions. The activation of multiple slip systems promotes frequent dislocation interactions and entanglements, contributing to strain hardening. Snapshots in Fig. 8 (with the full video provided in Video S2) show that dislocation rearrangements reduce the initially high dislocation density, resulting in the redistribution of internal stresses. After 25 s, this process reduces additional slip activity due to diminished driving stresses.

To directly compare the active mechanisms under different strain rates, we conducted an additional experiment at a high strain rate of 1 s^{-1}, keeping a maximum stress of ~350 MPa, well below the yield point at this strain rate. The sample was allowed to relax for 300 s while in situ TEM observations were conducted (Fig. 9). Snapshots were taken after 2 min, a timeframe that is needed to tilt samples to improved two-beam diffraction conditions and allowed for clear visualization of the active deformation process. Even at this lower stress level and later observation time, multiple slip systems remained active, similar to the higher stress case shown in Fig. 8. In contrast, the experiment conducted at a lower strain rate of 1×10^{-4} s^{-1} under the same stress level showed no activation of multiple slip systems, suggesting that multi-slip activity depends on both strain rate and stress history. Fig. 9 highlights dislocation interactions: a dislocation propagates along the direction indicated by arrow 1; a jog (arrow 2, see as well Video S3) on a dislocation slides orthogonally to the primary dislocation line; and a newly nucleated dislocation (arrow 3) travels along a distinct path. Based on Fig. 6, the measured V^* increases from 13 to $20b^3$ as the strain rate increases from 1×10^{-4} s^{-1} to 1 s^{-1}, indicating a clear strain rate dependence of activation volume. This trend further correlates with changes in active dislocation modes observed via in situ TEM straining, reflecting the combined influence of strain rate and stress history—leading to different dislocation structures and internal stress states—on plastic behavior. These results demonstrate that in situ TEM observations, coupled with quantitative measurements of activation volume, are essential to understanding the rate-controlling mechanisms, which are governed not only by external loading conditions but also by internal stress states (see the Discussion section), as evidenced by the transient dislocation dynamics and evolving dislocation structures observed through in situ TEM straining.

4. Discussion

In general, various deformation processes compete to determine the measured activation volume of a polycrystal as a function of strain rate, stress history, and grain size, etc. For instance, increasing strain rate can shift the rate-controlling deformation mechanisms. The increase in dislocation activity at higher strain rates, as captured by in situ TEM experiments, corresponds to the higher measured V^*. Conversely, at lower strain rates, the observed decrease of dislocation activity correlate

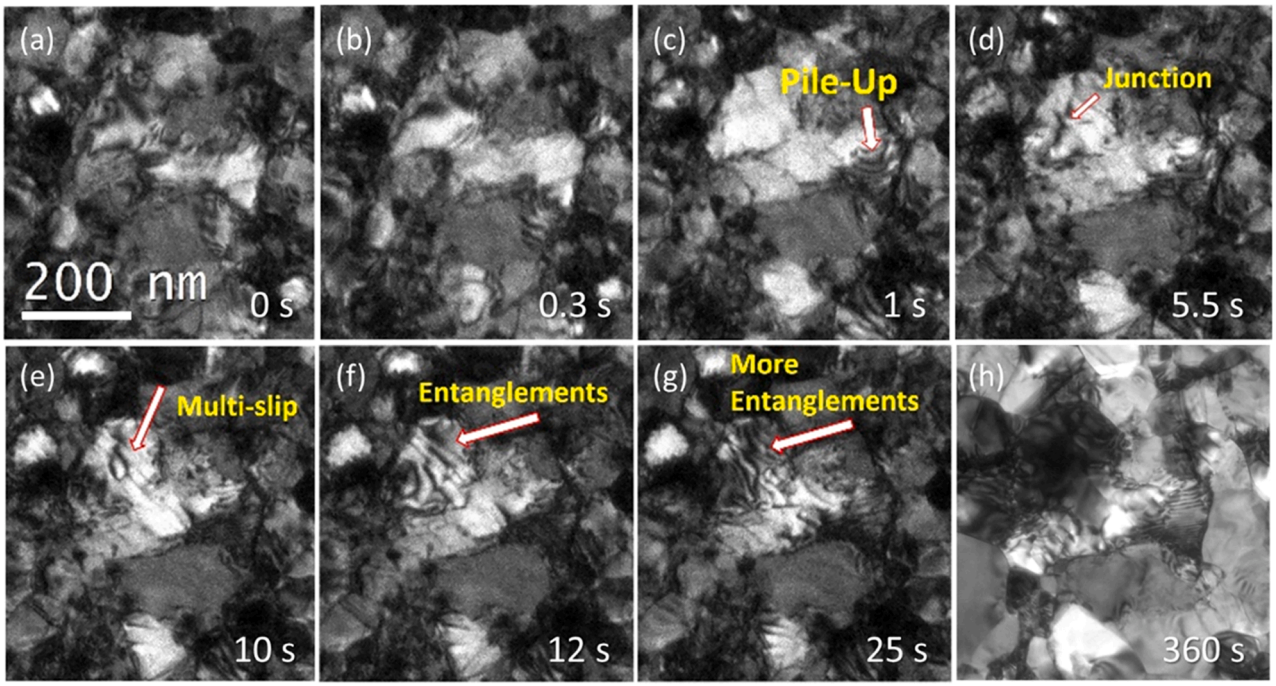

Fig. 8. In situ TEM images (a-h) capturing dislocation activity during the transient period after loading to 600 MPa at a high strain rate of 1 s^{-1}, revealing the onset of multiple slip systems. Orange outlines at the 360 s frame indicate the original GBs at the onset of the transient, and blue arrows indicate the directions of GB migration. (Available in Video S2).

with the lower measured V^*. To understand these results, we first discuss related studies in the literature and then develop a rate-dependent plasticity model to elucidate the competition between different rate-controlling mechanisms in UFG metals.

Wang and Hamza investigated deformation mechanisms in NC versus coarse-grained Ni and observed that the V^* in NC Ni was over one order of magnitude smaller than in bulk Ni [34]. Their results align with ours, as we consistently measured small V^* than those reported for bulk FCC metals [35,36]. Jonnalagadda et al. [25] studied similar UFG Au films as ours, but their films with larger thickness (1.76 μm) had smaller grain sizes of ~44 nm. While their smaller grain size would suggest a typically larger m value and thus a stronger influence of GB-mediated mechanisms, their reported upper bound m value (0.1) is lower than ours (0.16). This discrepancy indicates that factors beyond the area fraction of GBs, such as GB structure or grain size distribution, may play a significant role in governing the rate-limiting deformation mechanisms, and this will be the focus in our follow-up study. Apparent activation volumes V_a have also been reported, ranging from 4.5 to 8.1b^3 at lower strain rates (6×10^{-6} to 1×10^{-4} s^{-1}) and 12.5 to 14.6b^3 at higher strain rates (1×10^{-4} to 20 s^{-1}) [25]. However, V_a is an averaged macroscopic response that reflects the combined effects of various microstructural contributions, including dislocation density, and is therefore insufficient for pinpointing changes in rate-controlling deformation mechanisms. In contrast, the physical activation volume offers a more direct measure of the atomic-scale rate-limiting processes, enabling a clearer correlation with the underlying mechanisms.

Conrad advanced the understanding of plastic deformation kinetics in nanocrystalline FCC metals by developing a model that relates grain size to the relative contributions of intragranular and intergranular plastic deformation processes in determining the sample-level physical activation volume [23]. This model posits that stress concentrations arising from dislocation pile-up against GBs enhance the activation of plastic deformation within or near these boundaries. This interplay is mathematically represented by the following relation

$$\frac{1}{V^*} = \frac{1}{V_0^*} + \frac{M^2 \mu b}{2\pi\alpha K_{H-P}\sqrt{d}} \frac{1}{V_c} \tag{3}$$

where V^* is the physical activation volume of the polycrystalline sample, V_0^* is the activation volume associated with intragranular dislocation processes, and V_c represents the activation volume corresponding to GB-mediated processes. In Eq. (3), M is the Taylor factor, μ is the shear modulus, b is the Burgers vector length, α is a dimensionless constant, K_{H-P} is the Hall–Petch coefficient characterizing the relationship between grain size and yield strength, and d is the grain size. Since V_0^* scales with the spacing of dislocation obstacles within a grain, it tends to be relatively large, whereas GB-mediated processes are typically associated with smaller V_c values, often linked to atomic diffusion at GBs [23,37]. As grain size decreases, particularly in UFG and NC regimes, Eq. (3) suggests that GB-mediated mechanisms and their smaller V_c contribute increasingly to the sample-level activation volume V^*.

While Conrad's model captures key aspects of grain size-dependent activation volumes, our in situ TEM measurements reveal a more complex trend, identifying two distinct activation volumes: $8-14b^3$ and $6-20b^3$ depending on the applied strain rate (see Fig. 6). During our in situ TEM straining tests, we directly observed increased intragranular dislocation activity, such as multi-slip, at higher strain rates. Figs. 7–9 illustrate the combined effects of external loading conditions (e.g., strain rate and stress history) and internal stress states, evidenced by transient dislocation dynamics and evolving dislocation structures. These results indicate that while Conrad's model accounts for grain size effects, it does not fully capture the dynamic interplay between displacive and diffusive mechanisms in UFG metals. Our findings underscore the importance of incorporating both external and internal factors—and their interaction—when evaluating rate-limiting processes in these materials.

To address this discrepancy, we developed a rate-dependent plasticity model (detailed in the Supplementary Information) to elucidate the competition between rate-controlling mechanisms in UFG metals. Built upon conventional viscoplasticity theory, the model incorporates stress-dependent activation energy and accounts for the evolution of

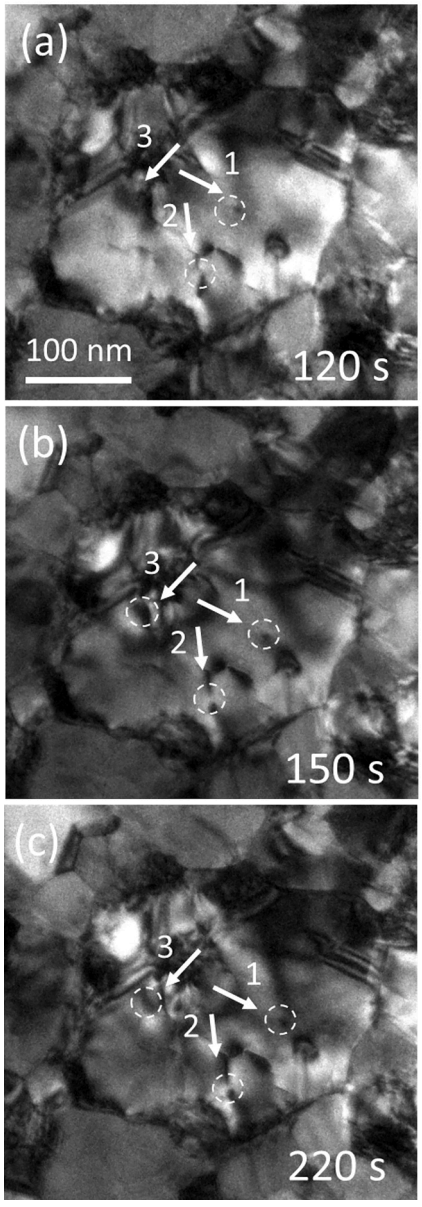

Fig. 9. In situ TEM images (a-c) showing dislocation activity during the transient period after loading to 350 MPa at a high strain rate of 1 s^{-1}. Arrows indicate different dislocations gliding on different slip planes. (Available in Video S3).

internal stresses through a back stress component governed by dislocation structures [38]. Numerical simulations from this model reproduce the experimental stress-strain responses and activation volumes across a wide range of strain rates. Two distinct parameter sets were required for low and high strain rates, respectively, indicating a transition between two different rate-limiting mechanisms. As shown in Fig. 10(a), the simulated stress-strain curves agree well with experimental measurements at both high (2.5×10^{-1} and 1.3×10^{-2} s^{-1}) and low (7.5×10^{-5} to 1.7×10^{-5} s^{-1}) strain rates. However, neither parameter set fully captures the response at an intermediate strain rate (3.5×10^{-3} s^{-1}), suggesting the combined effects of two competing mechanisms in this transitional regime. To further probe the rate-controlling mechanisms, we evaluated the activation volume from simulations using

$$V^*_{sim} = \sqrt{3}kT\frac{\partial \ln \dot{\varepsilon}_p}{\partial \sigma} \quad (4)$$

where $\dot{\varepsilon}_p$ is the plastic strain rate. As shown in Fig. 10(b), the simulated activation volumes V^*_{sim} match the experimentally measured V^* values under both high and low strain rates, reinforcing the presence of distinct dominant mechanisms in the high and low strain rate regimes.

The total flow stress comprises two components: (1) a temperature-insensitive long-range internal stress, such as the back stress arising from geometrically necessary dislocation accumulation at GBs and dislocation cells, and (2) a temperature-sensitive effective stress responsible for overcoming short-range obstacles. Under a given applied stress, the applied strain rate determines a specific combination of back stress and effective stress, which manifests in distinct dislocation dynamics and dislocation structures. This is because the effective stress activates a particular rate-controlling mechanism, each associated with a characteristic activation volume. The transition between two rate-controlling mechanisms with increasing strain rate is governed by their differing activation energy dependencies on effective stress. Fig. 10 (c) shows the activation energy versus effective stress curves for two competing mechanisms, corresponding to the two sets of parameters fitting the low and high strain rate regimes. The slope of each curve represents the activation volume. At any given effective stress, the mechanism with the lower activation energy is rate-controlling. A crossover between the two mechanisms occurs at 104 MPa (indicated by the vertical black line), marking the transition point. At an applied stress of 365 MPa (green dashed line in Fig. 10(b)), the model predicts the effective stresses of 87 MPa at 1.0×10^{-4} s^{-1} and 111 MPa at 1.0 s^{-1}, respectively. At the lower strain rate (1.0×10^{-4} s^{-1}), the mechanism with a lower activation energy at 87 MPa (marked by the dark yellow symbol in Fig. 10(c) is rate-controlling, resulting in a smaller measured activation volume of $13b^3$ In contrast, at the higher strain rate (1.0 s^{-1}), the alternative mechanism becomes rate-limiting due to its lower activation energy at 111 MPa (purple symbol in Fig. 10(c)), leading to a larger measured activation volume of $20b^3$ It should be noted that the present model captures the transition between two different rate-limiting processes, but does not explicitly resolve the relative contributions of intergranular versus intragranular processes, or diffusive versus displacive mechanisms. Further model development is needed to fully capture the complexity of rate-controlling mechanisms in UFG metals as a function of strain rate, stress history, and grain size.

5. Conclusions

This study investigates the plastic deformation kinetics of UFG Au thin films (100 nm thickness, 142 nm average grain size) using an integrated approach that combines in situ TEM observations of plastic deformation with MEMS-based measurements of physical activation volumes (V^*) over a range of strain rates (from 10^{-5} to 1 s^{-1}) that is wider than previously obtainable with this technique, thanks to the use of image-based sensing. Major findings are summarized as follows.

- The yield strength increases by a factor of three over four orders of magnitude in strain rate, whereas ductility diminishes markedly at higher strain rates.
- By correlating the mechanical testing results with in situ TEM observations at the same stress levels, we directly link the higher V^* measured at higher strain rates to the activation of multiple slip systems. In contrast, only single-slip activity is observed at lower V^* associated with lower strain rates.
- Combined experimental and modeling analyses reveal that the rate-controlling mechanisms are governed not only by the external loading condition but also by the internal stress state. This is evidenced by transient dislocation processes and evolving dislocation structures captured during observed in situ straining experiments.

Altogether, this study offers deeper insight into the rate-controlling mechanisms in UFG metals, and establishes an integrated

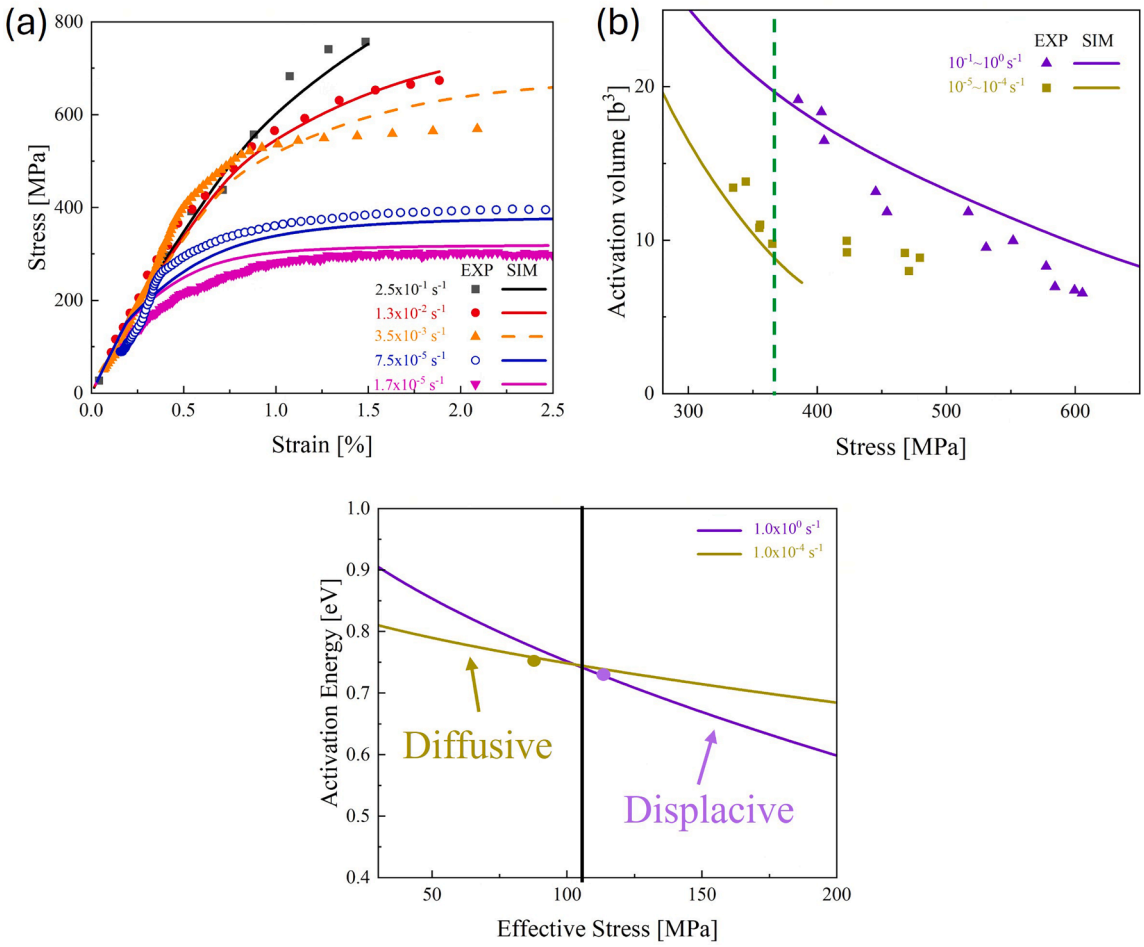

Fig. 10. Comparison of experimental and modeling results for uniaxial tension of UFG Au films under various strain rates. (a) Simulated and experimental results of stress strain curves at five different strain rates. (b) Simulated and experimental results of activation volume under high and low strain rates. (c) Modeled activation energy versus effective stress for two competing rate-controlling mechanisms. A crossover occurs at an effective of 104 MPa (vertical black line), marking the transition between the two mechanisms. At the same applied stress of 365 MPa, the dark yellow and purple symbols indicate the activation energies of the dominant mechanisms at low (1.0×10^{-4} s^{-1}) and high (1.0 s^{-1}) strain rates, respectively, with the corresponding low (87 MPa) and high (111 MPa) effective stresses.

experimental-modeling framework to further elucidate the competition of intragranular and intergranular mechanisms in advanced metallic materials.

CRediT authorship contribution statement

Yichen Yang: Writing – original draft, Validation, Investigation, Formal analysis, Conceptualization. **Kunqing Ding:** Writing – original draft, Formal analysis, Conceptualization. **Xing Liu:** Validation, Formal analysis, Conceptualization. **Ting Zhu:** Writing – review & editing, Supervision, Funding acquisition, Conceptualization. **Josh Kacher:** Writing – review & editing, Supervision, Funding acquisition, Conceptualization. **Olivier Pierron:** Writing – review & editing, Supervision, Funding acquisition, Conceptualization.

Declaration of competing interest

The authors declare that they have no known competing financial interests or personal relationships that could have appeared to influence the work reported in this paper.

Acknowledgements

The authors gratefully acknowledge support by the U.S. Department of Energy (DOE), Office of Science, Basic Energy Sciences (BES) Materials Science and Engineering (MSE) Division under Award #DE-SC0018960.

Supplementary materials

Supplementary material associated with this article can be found, in the online version, at doi:10.1016/j.actamat.2025.121868.

References

[1] H. Gleiter, Nanocrystalline materials, Prog Mater Sci 33 (4) (1989) 223–315.
[2] C.E. Carlton, P.J. Ferreira, What is behind the inverse Hall–Petch effect in nanocrystalline materials? Acta Mater 55 (11) (2007) 3749–3756.
[3] H. Conrad, J. Narayan, On the grain size softening in nanocrystalline materials, Scr Mater 42 (11) (2000) 1025–1030.
[4] Z. Jiang, Q. Wang, Y. Zhang, T. Suo, J. Wang, J. Liang, The deformation mechanism of nanocrystalline nickel under high strain rate, Mater Lett 305 (2021) 130790.
[5] K.S. Kumar, H. Van Swygenhoven, S. Suresh, Mechanical behavior of nanocrystalline metals and alloys11The Golden Jubilee Issue—Selected topics in Materials Science and Engineering: past, present and future, edited by S. Suresh, Acta Mater 51 (19) (2003) 5743–5774.
[6] I.A. Ovid'ko, R.Z. Valiev, Y.T. Zhu, Review on superior strength and enhanced ductility of metallic nanomaterials, Prog Mater Sci 94 (2018) 462–540.
[7] D. Wolf, V. Yamakov, S.R. Phillpot, A. Mukherjee, H. Gleiter, Deformation of nanocrystalline materials by molecular-dynamics simulation: relationship to experiments? Acta Mater 53 (1) (2005) 1–40.
[8] T. Zhu, J. Li, A. Samanta, H.G. Kim, S. Suresh, Interfacial plasticity governs strain rate sensitivity and ductility in nanostructured metals, Proc. Natl. Acad. Sci. 104 (9) (2007) 3031–3036.

[9] M.S. Colla, B. Amin-Ahmadi, H. Idrissi, L. Malet, S. Godet, J.P. Raskin, D. Schryvers, T. Pardoen, Dislocation-mediated relaxation in nanograined columnar palladium films revealed by on-chip time-resolved HRTEM testing, Nat. Commun 6 (2015) 8.
[10] H. Idrissi, A. Kobler, B. Amin-Ahmadi, M. Coulombier, M. Galceran, J.P. Raskin, S. Godet, C. Kubel, T. Pardoen, D. Schryvers, Plasticity mechanisms in ultrafine grained freestanding aluminum thin films revealed by in-situ transmission electron microscopy nanomechanical testing, Appl. Phys. Let 104 (10) (2014) 5.
[11] F. Mompiou, M. Legros, A. Boe, M. Coulombier, J.P. Raskin, T. Pardoen, Inter- and intragranular plasticity mechanisms in ultrafine-grained Al thin films: an in situ TEM study, Acta Mater 61 (1) (2013) 205–216.
[12] V. Samaee, R. Gatti, B. Devincre, T. Pardoen, D. Schryvers, H. Idrissi, Dislocation driven nanosample plasticity: new insights from quantitative in-situ TEM tensile testing, Sci Rep 8 (1) (2018) 12012.
[13] J.P. Liebig, M. Mackovic, E. Spiecker, M. Göken, B. Merle, Grain boundary mediated plasticity: a blessing for the ductility of metallic thin films? Acta Mater 215 (2021).
[14] P. Baral, A. Kashiwar, M. Coulombier, L. Delannay, K. Hoummada, J.P. Raskin, H. Idrissi, T. Pardoen, Grain boundary-mediated plasticity in aluminum films unraveled by a statistical approach combining nano-DIC and ACOM-TEM, Acta Mater 276 (2024) 120081.
[15] J. Lohmiller, M. Grewer, C. Braun, A. Kobler, C. Kübel, K. Schüler, V. Honkimäki, H. Hahn, O. Kraft, R. Birringer, P.A. Gruber, Untangling dislocation and grain boundary mediated plasticity in nanocrystalline nickel, Acta Mater 65 (2014) 295–307.
[16] G.J. Tucker, S. Tiwari, J.A. Zimmerman, D.L. McDowell, Investigating the deformation of nanocrystalline copper with microscale kinematic metrics and molecular dynamics, J. Mech. Phys. Sol 60 (3) (2012) 471–486.
[17] Y. Zhang, G.J. Tucker, J.R. Trelewicz, Stress-assisted grain growth in nanocrystalline metals: grain boundary mediated mechanisms and stabilization through alloying, Acta Mater 131 (2017) 39–47.
[18] A. Kobler, C. Brandl, H. Hahn, C. Kübel, In situ observation of deformation processes in nanocrystalline face-centered cubic metals, Beilstein J Nanotechnol 7 (2016) 572–580.
[19] S. Gupta, S. Stangebye, K. Jungjohann, B. Boyce, T. Zhu, J. Kacher, O.N. Pierron, In situ TEM measurement of activation volume in ultrafine grained gold, Nanoscale 12 (13) (2020) 7146–7158.
[20] S. Gupta, S. Stangebye, K. Jungjohann, B. Boyce, T. Zhu, J. Kacher, O.N. Pierron, In situ TEM measurement of activation volume in ultrafine grained gold (vol 12, pg 7146, 2020), Nanoscale 13 (19) (2021), 9040-9040.
[21] S. Stangebye, Y. Zhang, S. Gupta, T. Zhu, O. Pierron, J. Kacher, Understanding and quantifying electron beam effects during in situ TEM nanomechanical tensile testing on metal thin films, Acta Mater 222 (2022) 117441.
[22] P. Spätig, J. Bonneville, J.L. Martin, A new method for activation volume measurements: application to Ni3(Al,Hf), Mater. Sci. Eng.: A 167 (1) (1993) 73–79.
[23] H. Conrad, Plastic deformation kinetics in nanocrystalline FCC metals based on the pile-up of dislocations, Nanotechnology 18 (32) (2007) 325701.
[24] Y. Zhang, K. Ding, S. Stangebye, D. Chen, J. Kacher, O. Pierron, T. Zhu, Atomistic modeling of surface and grain boundary dislocation nucleation in FCC metals, Acta Mater 237 (2022) 118155.
[25] K. Jonnalagadda, N. Karanjgaokar, I. Chasiotis, J. Chee, D. Peroulis, Strain rate sensitivity of nanocrystalline Au films at room temperature, Acta Mater 58 (14) (2010) 4674–4684.
[26] N.J. Karanjgaokar, C.S. Oh, J. Lambros, I. Chasiotis, Inelastic deformation of nanocrystalline Au thin films as a function of temperature and strain rate, Acta Mater 60 (13–14) (2012) 5352–5361.
[27] S. Gupta, S. Stangebye, K. Jungjohann, B. Boyce, T. Zhu, J. Kacher, O. Pierron, In situ TEM measurement of activation volume in ultrafine grained gold, Nanoscale 12 (2020).
[28] S. Stangebye, X. Liu, L. Daza Llanos, Y. Yang, T. Zhu, J. Kacher, O. Pierron, Comparison of electrical sensing and image analysis for in situ transmission electron microscopy nanomechanical testing of thin films, Thin Solid Films 787 (2023) 140125.
[29] S. Gupta, O.N. Pierron, A MEMS tensile testing technique for measuring true activation volume and effective stress in nanocrystalline ultrathin microbeams, J. Microelectromechanical Syst. 26 (5) (2017) 1082–1092.
[30] S. Stangebye, K. Ding, Y. Yang, T. Zhu, O. Pierron, J. Kacher, Grain size effects on stress-assisted grain boundary migration in polycrystalline Au thin films under tension, Acta Mater 297 (2025) 121330.
[31] B. Pant, S. Choi, E. Baumert, B. Allen, S. Graham, K. Gall, O. Pierron, MEMS-based nanomechanics: influence of MEMS design on test temperature, Exper. Mech 52 (6) (2012) 607–617.
[32] S. Gupta, O. Pierron, A MEMS tensile testing technique for measuring true activation volume and effective stress in nanocrystalline ultrathin microbeams, J. Microelectromechanical Syst. 26 (5) (2017) 1082–1092.
[33] D. Caillard, J. Martin, Thermally activated mechanisms in crystal plasticity, Pergamon Mater. Ser. (2003).
[34] Y.M. Wang, A.V. Hamza, E. Ma, Activation volume and density of mobile dislocations in plastically deforming nanocrystalline Ni, Appl. Phys. Let 86 (24) (2005).
[35] M.J. Cordill, N.R. Moody, W.W. Gerberich, The role of dislocation walls for nanoindentation to shallow depths, Int. J. Plast. 25 (2) (2009) 281–301.
[36] F. Dalla Torre, P. Spätig, R. Schäublin, M. Victoria, Deformation behaviour and microstructure of nanocrystalline electrodeposited and high pressure torsioned nickel, Acta Mater 53 (8) (2005) 2337–2349.
[37] H. Conrad, Grain size dependence of the plastic deformation kinetics in Cu, Mater. Sci. Eng.: A 341 (1) (2003) 216–228.
[38] Y. Zhang, Z. Cheng, T. Zhu, L. Lu, Mechanics of gradient nanostructured metals, J Mech Phys Solids 189 (2024) 105719.